# Journal of Materials Chemistry A

Accepted Manuscript


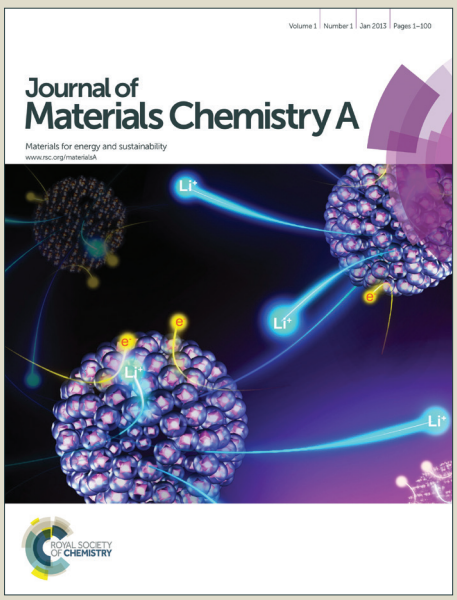





ROYAL SOCIETY OF CHEMISTRY

www.rsc.org/materialsA

Journal Name

ARTICLE

# An ingenious Ni/Ce co-doped titanate based perovskite as a coking-tolerant anode material for direct hydrocarbon solid oxide fuel cells

B Received 00th January 20xx,
Accepted 00th January 20xx

DOI: 10.1039/x0xx00000x

www.rsc.org/

Yi-Fei Sun,[a] Xin-Wen Zhou,[b] Yimin Zeng,[c] Babak Shalchi Amirkhiz,[c] Meng-Ni Wang,[a] Li-Zhong Zhang,[d] Bin Hua,[a,e] Jian Li,[e] Jian-Hui Li,[d,*] Jing-Li Luo[a,*]

For decades, Ni based cermet anode for solid oxide fuel cells (SOFCs) has been suffering from the poison of sulfur in fuel and carbon deposition while operating on hydrocarbon. Using perovskite as alternative can effectively alleviate these problem. However their performances are unsatisfying. In this work, a lanthanum strontium titanate based perovskite oxide with facile modification of Ni and Ce (LSCNT) was fabricated by a modified sol-gel method. The exsolution of Ni surrounded by uniformly dispersed Ce species in perovskite lattice could only be obtained by sintering the material in the consecutive atmospheres of air and 10% $H_2$/Ar. The solid oxide fuel cell (SOFC) equipped with an LSCNT anode exhibited desirable electrochemical performance and stability with 5000 pm $H_2S/H_2$ and dry methane fuel. The presence of exsolved metallic Ni provided strong active sites for the fuel oxidation reaction and simultaneously the Ce species with redox couple provided Ni with abundant oxygen ions. The synergetic effect between Ce and Ni facilitate the electrochemical reaction and promote the removal of carbon deposition. All these features make LSCNT a promising sulfur and carbon-deposition tolerant anode material for SOFCs.

## Introduction

The discovery of highly efficient, stable, and fuel-flexible anode materials for solid oxide fuel cells (SOFCs) is still a big challenge. Promising alternative materials must obtain electrochemical performance comparable to traditional Ni based cermets, and also must be robust in a sour atmosphere and have tolerance against coking. [1-6]

Perovskite families have been widely investigated as potential replacements for Ni-yttria stabilized zirconia (YSZ) cermets. [7-13] Among various candidates, titanates, especially the doped $SrTiO_3$ have been considered because of their stability in sour and reducing atmospheres. The doping with trivalent ions such as $La^{3+}$ has been suggested as an effective way to enhance the ionic conductivity of the material.[8] Under a reducing atmosphere, the presence of trivalent ions facilitates the reduction of $Ti^{4+}$ to $Ti^{3+}$ and further enhances the electronic conductivity.[14] However, despite of these desirable electrical properties, the industrial application is still restricted by their low catalytic activity.

To enhance the performance of the anode materials, without using traditional impregnation methods that generate nonhomogeneous dispersed active particles,[15] catalytically active elements were dissolved in fabricated perovskite lattices then exsolved in a reducing atmosphere.[16] Nanoparticles prepared by this method suffered less from coking due to their fine dispersion.[17]

The stable fluorite structure of cerium oxide can obtain the desired level of oxygen storage.[18] A reducing atmosphere creates oxygen vacancies in cerium oxide, and the deficient material can capture oxygen ions in the surrounding environment to be reoxidized to $CeO_2$.[19] Cerium based compounds are of interest in solid oxide fuel cells that are directly operated on methane[20] as well as in catalysis reforming reactions.[21,22] The cerium based compounds exhibited the ability of tolerance against carbon deposition[23]. Also, detailed investigation showed that, unlike another effective carbon deposition resistance promoter of copper which did not catalyse the formation of C-C bond,[24] the cerium based compound displayed the catalytic activity for combustion of carbon. The addition of cerium oxide to lanthanum doped strontium titanate (LST) based perovskite has been found to improve fuel cell performance without carbon deposition even under critical coking conditions.[25] In composites with isolated $CeO_2$ and LST, the addition of $CeO_2$

[a] Department of Chemical and Materials Engineering, University of Alberta, Alberta, Canada, T6G 2V4.
[b] College of Biological and Pharmaceutical Science, China Three Gorges University, Yichang, China, 443002.
[c] Canmet MATERIALS, Natural Resources Canada, Hamilton, Ontario, Canada, L8P 0A5.
[d] National Engineering Laboratory for Green Chemical Productions of Alcohols-Ethers-Esters, College of Chemistry and Chemical Engineering, Xiamen University, Xiamen, China, 361005.
Present Address: Department of Chemistry and Applied Chemistry, Changji University, Changji, China, 831100.
[e] Center for Fuel Cell Innovation, School of Materials Science and Engineering, State Key Laboratory of Material Processing and Die & Mould Technology, Huazhong University of Science and Technology, Wuhan, China, 430074.

enhanced the methane steam reforming reaction by one order of magnitude compared to the pure LST catalyst.[26] Zhou et al. also found that exsolution of $CeO_2$ could improve the oxidation of hydrogen in SOFCs with a Ba doped LST (LSBT) anode compared to pure LSBT and to LSBT mechanically mixed with $CeO_2$.[27]

Perovskite was also doped with oxides of catalytically active elements such as Ru, Pd, and Ni, in addition to $CeO_2$, which could sharply decrease the activation polarization resistance of the anode due to the exsolution of corresponding nanoparticles.[28-30] Although the electrochemical performance of these composites has been studied, their sulfur and coking resistances have not been fully demonstrated. Therefore, it is of great significance to develop an anode material that possesses a combined property of good sulfur tolerance, coking resistance, and catalytic activity. Best to our knowledge, so far no report has been shown on the synergistic effect of exsolved Ni and $CeO_2$ on perovskite anode.

In this work, we first utilized a modified sol-gel method to fabricate a novel composite anode consisting of an LST matrix with homogeneously dispersed metallic Ni particles enclosed by $CeO_2$. The LSCNT composite anode has demonstrated superior catalytic activity, good sulfur tolerance, and coking resistance. The important roles affecting the performance and carbon tolerance of the material were also studied.

## Experimental

### Materials Fabrication

$La_{0.3}Sr_{0.6}Ce_{0.1}Ni_{0.1}Ti_{0.9}O_{3-\delta}$ (LSCNT) and $La_{0.4}Sr_{0.6}Ni_{0.1}Ti_{0.9}O_{3-\delta}$ (LSNT) perovskite nanopowders were prepared using a modified sol-gel method. Stoichiometric amounts of $La(NO_3)_3 \bullet 6H_2O$, $Ce(NO_3)_3 \bullet 6H_2O$, $Sr(NO_3)_2 \bullet 6H_2O$, $Ni(NO_3)_2 \bullet 6H_2O$, $Ti(OC_3H_7)_4$, and citric acid ($C_6H_8O_7$) were sufficiently ground at room temperature. During the grinding process, $Ti(OC_3H_7)_4$ started to hydrolyze, accompanied by the evaporation of propyl alcohol and nitrogen oxides. An appropriate quantity of deionized water was added to accelerate the hydrolysis of $Ti(OC_3H_7)_4$ and accommodate the conglutination resistance. The obtained rheological phase material was then transferred into a container, sealed, and placed in a stainless autoclave at 120 °C for 12 h. The precursor calcined at 1200 °C for 10 h in air was denoted as A-LSCNT. Also, the precursor was calcined in the atmosphere of 10% $H_2$/Ar (Praxair) at 1200 °C for 10 h to form the powder denoted as H-LSCNT. Similarly, the precursor was firstly sintered at 1200 °C for 10 h in air, after that, the gas was shifted to 10% $H_2$/Ar (Praxair) for another 10 h. the sample formed was denoted as LSCNT. The detailed denotation of each sample could be found in Table 1 below.

**Table 1.** Designation of various materials

| Denotation | Composition | Calcination atmosphere |
|---|---|---|
| A-LSCNT | $(La_{0.3}Sr_{0.6}Ce_{0.1})(Ni_{0.1}Ti_{0.9})O_{3-\delta}$ | Air |
| H-LSCNT | $(La_{0.3}Sr_{0.6}Ce_{0.1})(Ni_{0.1}Ti_{0.9})O_{3-\delta}$ | 10% $H_2$/Ar |
| LSCNT | $(La_{0.3}Sr_{0.6}Ce_{0.1})\ (Ni_{0.1}Ti_{0.9})O_{3-\delta}$ | Air, then 10% $H_2$/Ar |
| LSNT | $(La_{0.4}Sr_{0.6})\ (Ni_{0.1}Ti_{0.9})O_{3-\delta}$ | Air, then 10% $H_2$/Ar |
| LSCT | $(La_{0.3}Sr_{0.6}Ce_{0.1})TiO_{3-\delta}$ | Air, then 10% $H_2$/Ar |

### Fuel cell fabrication

Fuel cells were fabricated using commercial YSZ disks with 300 μm in thickness and 25 mm in diameter (FCM, "fuelcellmaterials.com") as electrolyte. The cathode was a mixture of equal weights of YSZ powder (TOSHO Co. Ltd.) and strontium doped lanthanum manganese (LSM). The anode was prepared by mixing equal weights of YSZ and prepared anode materials. Both cathode and anode inks were prepared from oxide powders dispersed in terpineol mixed with 10% polyethylene glycol (PEG) as a screen printing binder. The electrode inks were deposited onto the YSZ electrolyte disc using screen printing to form a membrane electrode assembly (MEA) with an area of 1 $cm^2$, then the cell was sintered at 1100 °C for 2 h to form good binding between the electrodes and the electrolyte. The cathode and anode sides were painted with platinum paste and gold paste, respectively, to serve as the current collectors.

Single cell tests were performed in a vertical furnace with a coaxial two-tube (inlet and outlet) set-up. The outlet tube was directly sealed (Ceramabond 503, Aremco Products) to the outer edge of the anode side of the single cell electrolyte to avoid leakage of fuel gas and oxygen. A Thermolyne F79300 tubular furnace was used to heat the cell. As the fuel, hydrogen or hydrogen mixed with 5000 ppm $H_2S$ (5000 ppm $H_2S/H_2$) (Praxair) and dry methane was fed at a rate of 75 mL $min^{-1}$. The electrochemical performance of the fuel cell was measured using a Solartron 1287 instrument with a 2588 frequencer. The polarization resistance of the cell was estimated based on electrochemical impedance spectroscopy (EIS) measured at the open circuit voltage with an AC potential signal of ± 10 mV amplitude and a frequency range of 1 MHz to 0.1 Hz.

### Materials characterization

The phase structures of synthesized materials were characterized using a Rigaku Rotaflex X-ray diffractometer (XRD) with Cu Kα radiation and the data obtained were analyzed using JADE 5.0 software.

Pulse reaction experiments were carried out on an autosystem with an online gas chromatograph (HP 5890) equipped with a thermal conductivity detector (TCD). Using a six-way valve, a fixed amount of 0.20 mL of methane, or oxygen/helium ($O_2$/He = 1/9) was introduced into the carrier gas (He) flowing through the catalyst bed, which was held at 800 °C.

Hydrogen temperature programmed reduction ($H_2$-TPR) was performed using an AutoChem II 2920 instrument (Micromeritics, USA) equipped with an thermal conductivity detector (TCD). All samples were treated with Helium at 1000 °C for 30 min before TPR. The flow rate for analysis is 10%

$H_2$/Ar = 10 mL $min^{-1}$ and the temperature ramping rate is 10 °C $min^{-1}$.

The temperature-programmed oxidation (TPO) method was adopted to characterize and quantify the carbon deposition on the anode materials after various treatments. The samples were put in an alumina tube, loaded into the TPO apparatus and exposed to a flow of 10% $O_2$ balanced with He at 50 ml $min^{-1}$ for 1 h. The temperature was then increased from room temperature to 900 °C at 20 °C $min^{-1}$ in air and $CO_2$, and the effluents were analyzed by the mass spectrometer (Thermo star 301). Signals for m/z = 44 ($CO_2$), m/z = 28 (CO only, the residual $N_2$ contribution and $CO_2$ contribution to 28 were removed from analysis), m/z = 32 ($O_2$) and m/z = 18 ($H_2O$) were monitored during the TPO experiment. Prior to the TPO analysis, the mass spectrometer signals had been calibrated using gas mixtures of known concentrations.

The micromorphology of the materials was examined using a JEOL 6301F Scanning Electron Microscope (SEM) with an energy-dispersive x-ray (EDX) detector.

TEM study was done using FEI's Tecnai Osiris TEM equipped with X-FEG gun at 200 keV. High angle annular dark field (HAADF) with EDX elemental mapping was used to identify the chemistry of the samples.

## Results

### Textural and Structural Properties

Figure 1 shows XRD patterns of LSCNT powders sintered in various conditions. It can be seen that the H-LSCNT powder presents a cubic perovskite structure similar to $SrTiO_3$ with two diffraction peaks belonging to metallic Ni located at 44° and 52°,[31] suggesting that the doping of Ni in a perovskite lattice can be reduced in a reducing atmosphere. In comparison, the A-LSCNT powder exhibits the pure perovskite structure combined with peaks attributed to $CeO_2$, demonstrating that Ce cannot totally dissolve into perovskite lattice in the air atmosphere. Similar phenomena were observed in the synthesis of $La_{0.3}Ce_{0.1}Sr_{0.5}Ba_{0.1}TiO_3$ material, where cubic $CeO_2$ could be detected.[27] For LSCNT materials, diffraction peaks attributed to Ni and only one peak of $CeO_2$ could be found (see Figure 1(b)). So, we speculated that the reducing atmosphere in the second step help the further dissolution of Ce in perovskite lattice. However, detectable amount of $CeO_2$ still could be found. The Rietveld refinement method (RIR method) was employed to calculate the weight percentage of undissolved $CeO_2$ of 0.82 wt% (Considering that the RIR value of $CeO_2$=13.2 and the RIR value of perovskite is 6.22). The theoretical calculated weight percentage of Ce in LSCNT perovskite is 6.6 wt%. Consequently, the quantity of undissolved $CeO_2$ is estimated to be around 12.4%.

The phase of LSNT was also analyzed by XRD for comparison. The pure LSNT sample sintered in air at 1200 °C for 10h showed pure perovskite structure without impurity. After that, the sample was further sintering in 10%$H_2$-$N_2$ at 1200 °C for 10h. The XRD result showed the diffraction peaks belonging to metallic Ni. So we inferred that the Ni dissolve into the lattice in the first sintering process and exsolved out in the second step.

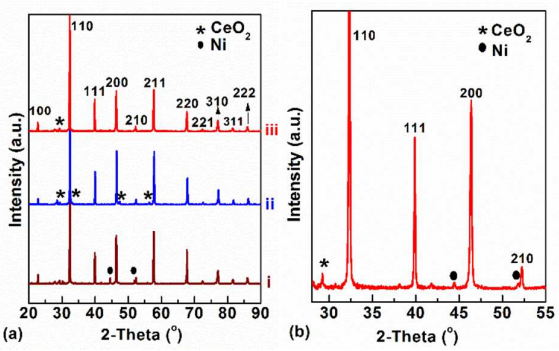


**Figure 1.** (a) XRD patterns of (i) H-LSCNT, (ii) A-LSCNT, and (iii) LSCNT; (b) low rate scan XRD pattern for sample LSCNT from 25 – 55°.

Figures 2(a) and 2(b) exhibit SEM images of the cross-section and surface of the cell, respectively, before the fuel cell test. It is clearly shown that the combination of anode and electrolyte is compact and the anode thickness is around 60 µm. The images also illustrate that LSCNT and YSZ are mixed well and the particle size distribution is uniform. SEM images 2(c) and 2(e) show that the exsolved particles are dispersed evenly with an average size of 200 nm.

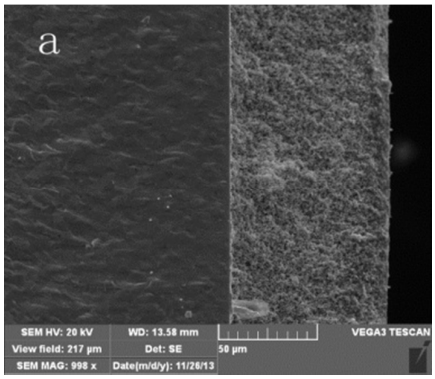


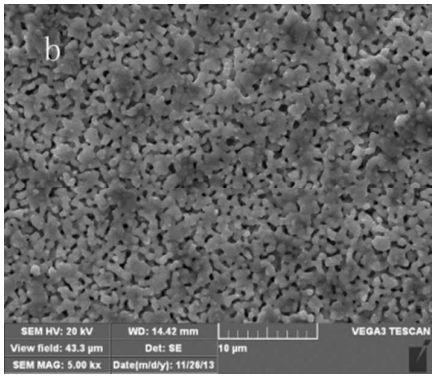

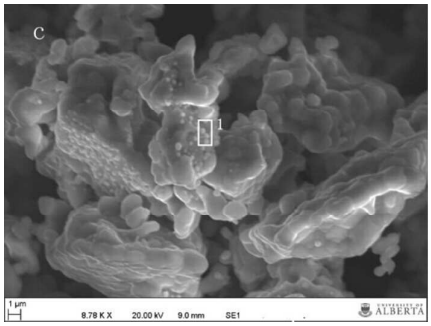


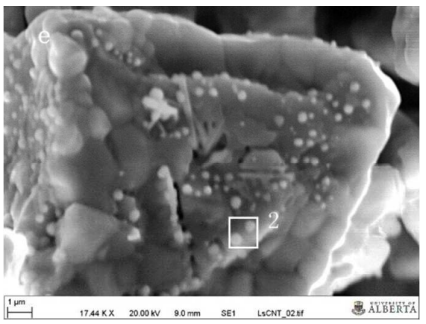


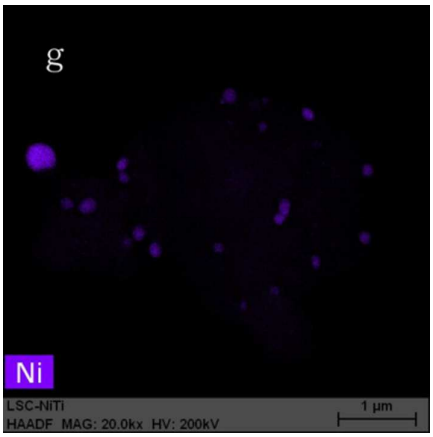


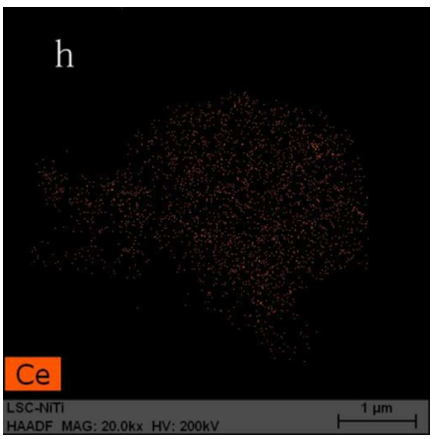


**Figure 2.** SEM images of (a) a cross section and (b) the surface of a typical cell with an LSCNT anode before a fuel cell test. SEM images of the exsolution of particles on fresh LSCNT powder are shown in (c) and (e). EDX line scans of the exsolved particles are shown in (d) and (f). HAADF image of the material overlaid with EDX elemental map of Ni highlighting nanoparticles (g) and Ce elements (h).

The composition of exsolved particles on the LSCNT anode was analyzed by EDX line scans crossing several particles and the results are shown in Figures 2(d) and 2(f). Here, to quantitatively describe the variation in concentration of each element, five zones corresponding to dramatic changes in the signal intensity for each element (La, Sr, Ce, Ni, Ti) were selected for detailed investigation. The Ni signal increased sharply on each particle, indicating that the exsolved particles should be metallic Ni.

The HAADF image of the material overlaid with EDX elemental map of Ni-highlighting nanoparticles is shown in Figure 2 (g). The presence of homogeneously dispersed bright spots with pretty high density should be corresponding to the exsolved Ni nanoparticles on the perovskite matrix. Also, the well dispersion of Ce on the perovskite scaffold can be indicated and the result is shown in Figure 2(h). The $CeO_2$ exhibits no segregation on the surface of the material and evenly enclose the exsolved Ni particles.

**Electrochemical performances in 5000 ppm $H_2S/H_2$**

Voltage versus current and power density curves of single fuel cells with LSCNT or LSNT anodes operated at different temperatures using 5000 ppm $H_2S/H_2$ as fuel are presented in Figures 3(a) and 3(b), respectively. As the temperature increased from 800 °C to 900 °C, the maximum power density (MPD) of cells with LSCNT increased from 260 mW $cm^{-2}$ to 660 mW $cm^{-2}$ and the corresponding current density increased from 1100 mA $cm^{-2}$ to 2600 mA $cm^{-2}$. These results are much higher than those achieved with cells with LSNT anodes which obtained an MPD of 330 mW $cm^{-2}$ at 900 °C. Previous research by our group showed that a cell with a $La_{0.3}Ce_{0.1}Sr_{0.5}Ba_{0.1}TiO_3$ (LSCBT) anode on which the exsolution of nano-$CeO_2$ could be found exhibited an MPD of only 110 mW $cm^{-2}$.[27] A comparison of the electrochemical performance of different anodes indicates that the doping of both Ni and Ce can improve the catalytic activity of the anode material and there probably is a synergetic effect between these two elements.

Figures 3(c) and 3(d) display electrochemical impedance spectra (EIS) data for LSCNT and LSNT anodes under open circuit voltage (OCV) at different temperatures. The interception of the curve on the X-axis corresponds to the ohmic resistance of the cell and the diameter of the semicircle between high frequency and low frequency can be ascribed to the activation polarization resistance (APR) of the electrode.[9] At 800 °C, for instance, the cell with an LSCNT anode shows an ohmic resistance of 0.32 Ω $cm^2$ and an APR of 0.45 Ω $cm^2$. We fabricated the symmetrical half-cell with the configuration of LSM/YSZ/LSM by the same method we used to fabricate single cell and tested its polarization resistance in the air at elevated temperature. The results showed that the LSM cathode exhibited activation polarization of around 0.19 Ω $cm^2$ at 800 °C,which are similar to the what had been reported before.[32, 33] So the calculated APR of the LSCNT anode is around 0.26 Ω

cm$^2$, which is lower than the 0.82 Ω cm$^2$ of the LSNT anode and comparable to the conventional Ni/YSZ cermets anode[3] and Ni modified YST/YSZ anode[34] using wet $H_2$ as fuel.

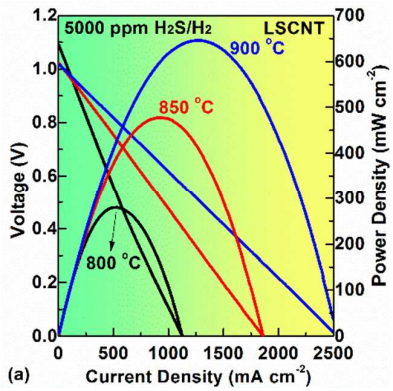


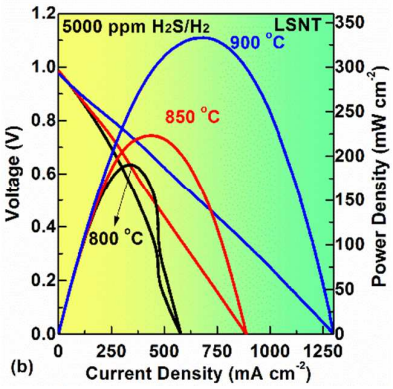


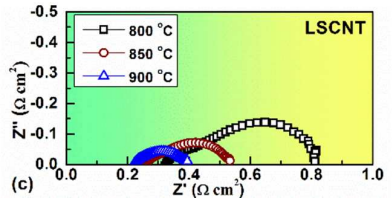


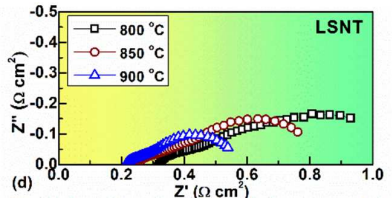


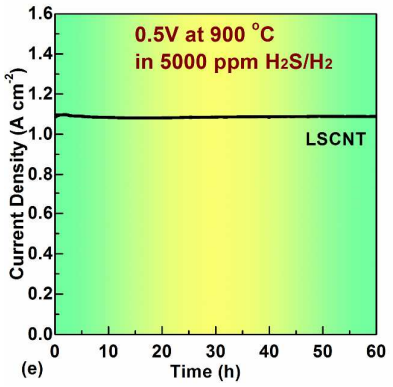


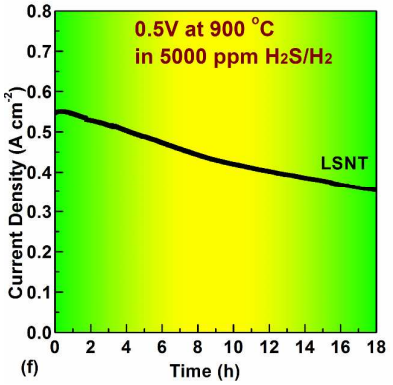


**Figure 3.** Current density vs. voltage and power density curves of fuel cells with (a) LSCNT and (b) LSNT anodes at different temperatures fed with 5000 ppm $H_2S/H_2$. Electrochemical impedance spectra (EIS) of fuel cells with (c) LSCNT and (d) LSNT anodes at different temperatures fed with 5000 ppm $H_2S/H_2$. A short-term stability test of cell with (e) LSCNT and (f) LSNT in 5000 ppm $H_2S/H_2$ at 900 °C.

The cell with the LSCNT anode was exposed to 5000 ppm $H_2S/H_2$ for the short-term stability test, see Figure 3(e). At 900 °C the cell exhibited excellent stability at 0.5 V with a stable current density output of around 1.1 A cm$^{-2}$ for 60 hours of operation without any degradation, suggesting that the anode materials had desirable sulfur tolerance. However, the good sulfur resistance only is not the ultimate assessment of an anode's stability. Unfortunately, we cannot conduct the stability test in sour hydrocarbon fuel due to the limitation of experiment condition. We will try to test it in the future. The short-term stability of the cell with LSNT anode in sour gas at 900 °C was also performed in order to have good comparison with LSCNT cell. It was shown in Figure 3(f) that at 0.5 V and 900 °C, the stability of LSNT in sour $H_2$ is not satisfying, the current density of which dropped sharply from 0.55 A cm$^{-2}$ to 0.35 A cm$^{-2}$, indicating that the sulphur resistance of LSNT is poor.

**Electrochemical performances in dry methane**

The electrochemical performance of LSCNT and LSNT anodes in dry methane at 900 °C was tested and the results are shown in Figure 4. The cell with an LSCNT anode exhibited superior

catalytic activity for the oxidation of methane, generating an MPD of ~ 600 mW $cm^{-2}$ at 900 °C which is almost three times higher than that of the cell with an LSNT anode. Stability tests for both cells in dry $CH_4$ at 900 °C are shown in Figure 4(b). It is obvious that the LSCNT anode demonstrated better coking resistance than the LSNT anode. At a voltage of 0.5 V, the cell with an LSCNT anode displayed an increasing current density for the first 60 hours of the test. Subsequently, the cell generated a stable current density of around 0.75 A $cm^{-2}$. Conversely, the current density in the cell with an LSNT anode decreased by 15%, from 0.4 A $cm^{-2}$ to 0.34 A $cm^{-2}$.

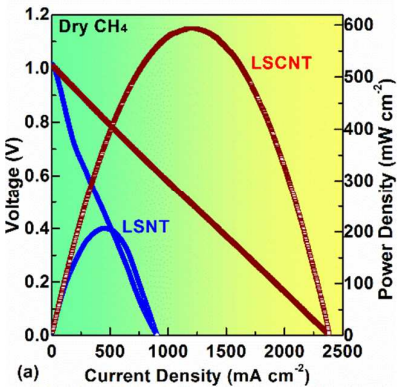


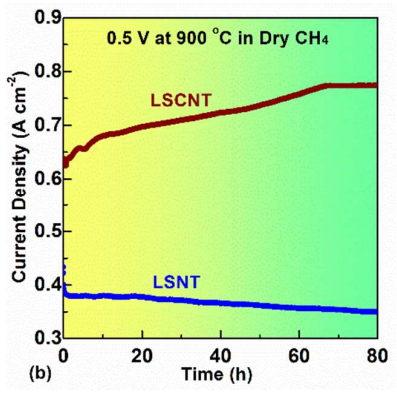


**Figure 4.** (a) Voltage and power density vs. current density and (b) current density vs. time (stability test) of fuel cells with LSCNT or LSNT anodes at 900 °C in dry $CH_4$.

According to previous research, carbon deposition can easily build up on a Ni-based anode when the cell is fed with dry $CH_4$;[35, 36] carbon deposition can lead to degradation of the LSNT anode. The addition of Ce to LSNT can effectively alleviate performance degradation through several pathways. We found that $CeO_2$ doping of the $La_{0.4}Sr_{0.5}Ba_{0.1}TiO_3$ (LSBT) anode could increase the removal of carbon deposition formed during the reaction.[7] Another study showed that Ce doping in the $La_{0.7}Sr_{0.3}Fe_{0.5}Cr_{0.5}O_{3-d}$ (LSFC) anode can create more available oxygen vacancies in the lattice, enhancing oxygen mobility, which promotes cell performance as well as the regenerability of the cell from coking.[37] Yu also reported that $Sm_{0.2}(Ce_{1-x}Ti_x)_{0.8}O_{1.9}$ effectively prevented methane fuel from directly impacting the Ni/YSZ anode, thereby enhancing tolerance to carbon deposition. Other experiments need to be applied to investigate the role Ce plays in the LSCNT anode.

## Discussion

In our investigation, the LSCNT anode with exsolution of Ni and uniformly dispersed Ce species exhibited superior performance compared to the LSNT anode. Because of the synergy between metallic Ni and Ce species, the LSCNT anode displayed high performance, good carbon and sulfur resistance running in dry methane.

The direction and comprehensive comparison of maximum powder density of cells with different anodes was shown in Figure 5. It could be clearly seen from the chart that the LSCNT anode exhibited best performance in both 5000 ppm $H_2S/H_2$ ppm and dry methane among three anode candidates. It has the MPD of almost 600 mW $cm^{-2}$ in dry methane, which is three times higher than LSNT and approximate six times higher than LSCT.

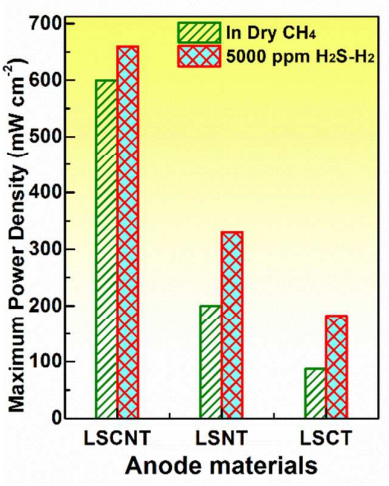


**Figure 5.** The comparisons of the maximum power density output of LSCNT, LSNT and LSCT with various fuels.

First, the additive Ce species promoted the electrochemical performance of the cell by offering more active oxygen ions. The results of the pulse experiments carried out at 800 °C are shown in Figures 6(a) and 6(b). In the methane pulse experiment, only $CO_2$, CO, and $H_2O$ were produced over the catalysts we studied. It is clear that LSCNT and LSNT differ considerably in methane oxidation activity. In the LSNT anode, the conversion of $CH_4$ decreased sharply from 75% to 5% after three pulses, suggesting that there was a limited quantity of active oxygen species in the sample. Previous research on Ni based catalysts determined that the quickly consumed active species come from the nonstoichiometric oxygen over the catalyst surface [38]. With the addition of Ce species in the lattice, the LSCNT catalyst showed a significantly higher

conversion of methane. The conversion decreased gradually from 89% to 14% with an increasing pulse number from 1 to 10, as opposed to the sharp decline observed in the LSNT catalyst. Therefore, Ce redox couple doping of the anode created more active oxygen species, facilitating the conversion of methane.

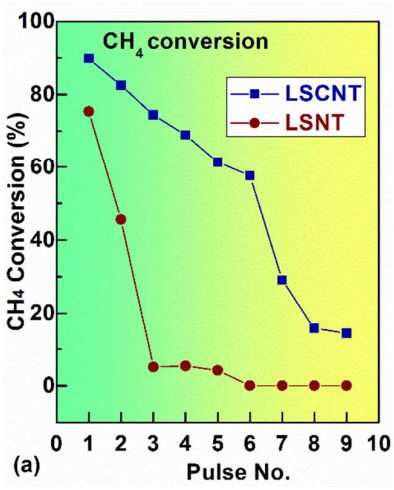


**Figure 6.** Pulse experiments on LSCNT and LSNT catalysts: (a) $CH_4$ conversion with methane pulses; (b) $O_2$ conversion with oxygen pulses.

The oxygen pulse experiment was performed after 10 methane pulses over the catalysts; the results are shown in Figure 6(b). The difference in LSCNT and LSNT curves reveals that the overall oxygen consumption of the LSCNT anode was much higher than that of the LSNT anode, in agreement with the cases shown in Figure 5(a), where higher methane conversion and much more oxygen depletion was observed on the LSCNT anode than on the LSNT anode. These results indicate that Ce doped LSCNT exhibits desirable redox properties, that is, LSCNT can be reduced and re-oxidized easily.

The activity of oxygen species and the corresponding oxygen storage capacity and redox capability of LSCNT and LSNT catalysts were investigated using temperature programmed reduction (TPR), in which samples were heated to 800 °C in 5% $H_2$/Ar. As shown in Figure 7(a), the hydrogen uptake was greater from the LSCNT sample than from the LSNT sample. This difference indicates that Ce doping of LSNT facilitates the reduction of bulk oxygen ions, which increases the oxidation of fuel. After being purged with He, LSCNT and LSNT samples were subjected to $O_2$-temperature programmed oxidation ($O_2$-TPO) to evaluate the redox reversibility of the materials. The experiment was conducted by heating the samples to 800 °C in air at 5 °C $min^{-1}$. Figure 7(b) shows the oxygen absorption versus temperature of LSCNT and LSNT samples. The oxygen uptake of LSCNT was approximately the same as the hydrogen uptake in the $H_2$-TPR analysis, which was much higher than that of LSNT; therefore, the redox reversibility of LSCNT is desirable.

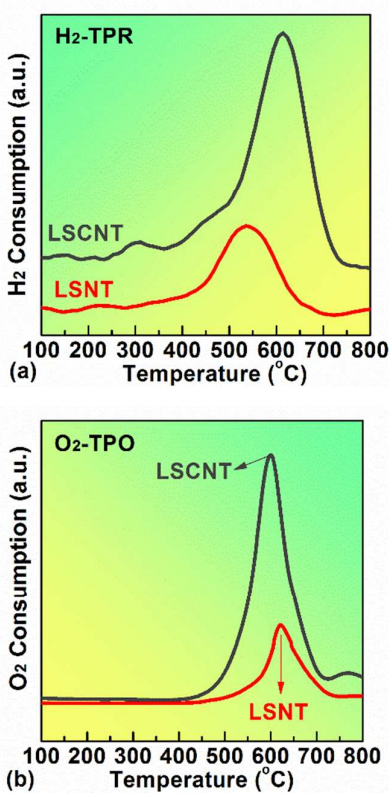


**Figure 7.** (a) Temperature programmed reduction (TPR) and (b) temperature programmed oxidation (TPO) of LSCNT and LSNT materials.

Second, the addition of Ce species significantly suppressed carbon deposition and enhanced the stability of the LSNT and LSCNT fuel cells. Sequential $CO_2$-TPO/$O_2$-TPO tests were performed to study the reactivity of carbon deposition on the anode catalysts after stability tests in methane; the results are shown in Figure 8. Reddy reported that filamentous carbon

could be removed by $CO_2$, but amorphous-like carbon could not be readily oxidized by the weak oxidant $CO_2$.[39] Consequently, we believed that carbon species that could be oxidized by $CO_2$ must be filamentous carbon, as shown in Figure 8(a). After the $CO_2$-TPO experiment and temperature reduction to room temperature in Ar at 5 °C $min^{-1}$, both amorphous and filamentous carbon samples were subjected to $O_2$-TPO analysis. The carbon deposition in Figure 8(b) can be assigned to the amorphous carbon which can be oxidized only by $O_2$. Both materials exhibit two $CO_2$ peaks which shows that $CO_2$ has different interactions with the surface of the LSCNT anode. With the addition of Ce species, the position of $CO_2$ peaks shifts to lower temperature. In addition, the intensity of the higher temperature peak became much weaker, and the formation of carbon, which can be oxidized at low temperature, was facilitated. The peak intensity ratio of lower temperature one to high temperature one is 9.9% and 37.2% for LSNT and LSCNT, respectively. Therefore, it can be inferred that the presence of Ce suppressed carbon deposition and increased the removal of deposited carbon.

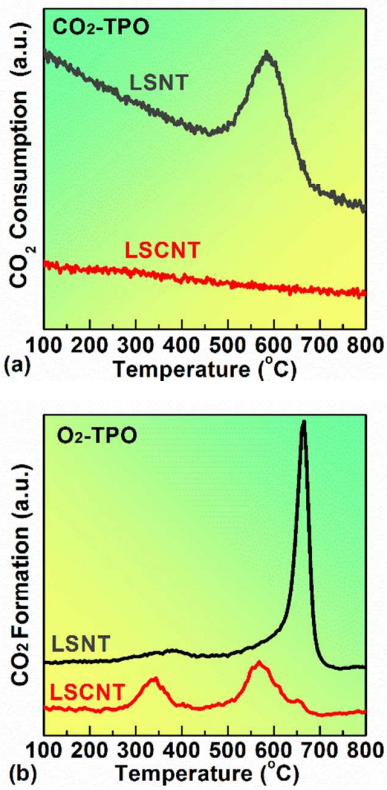


**Figure 8.** Sequential (a) $CO_2$-TPO consumption and (b) $O_2$-TPO formation in LSNT and LSCNT cells after stability tests in dry methane.

Several reactions (eq. 1–4) could facilitate carbon deposition on LSNT and LSCNT anodes. A schematic representation of carbon formation pathways is shown in Figure 9(a).

$$CH_4 \rightarrow C + H_2 \quad (1)$$

$$2CO \rightarrow CO_2 + C \quad (2)$$

$$H_2 + CO \rightarrow H_2O + C \quad (3)$$

$$2H_2 + CO_2 \rightarrow 2H_2O + C \quad (4)$$

At 900 °C, carbon would deposit mainly via the decomposition of methane (eq. 1) which has a Gibbs free energy of -38.01 kJ $mol^{-1}$. It is generally accepted that the $CH_4$ molecules decomposed on the Ni surface to form reactive species $CH_x$ (x = 0–3) that could be sources of carbon deposition.[40] Possible reactions between these intermediate surface hydrocarbon species are represented in eq. 5–9:

$$CH_4 + A \rightarrow CH_3\text{-}A + H\text{-}A \quad (5)$$

$$CH_3\text{-}A + A \rightarrow CH_2\text{-}A + H\text{-}A \quad (6)$$

$$CH_2\text{-}A + A \rightarrow CH\text{-}A + H\text{-}A \quad (7)$$

$$CH\text{-}A + A \rightarrow C\text{-}A + H\text{-}A \quad (8)$$

where A is the active site of the reaction. By doping LSNT with Ce species, a promoter that has uniform dispersion in the perovskite lattice, carbon deposition could be partially inhibited by gas–solid reactions between hydrocarbons and lattice oxygen ($O_x$) at the $CeO_2$ surface, forming hydrogen and carbon dioxide which are thermodynamically favored (eq. 9–10). These two processes are promoted in the presence of uniformly dispersed Ce species surrounding Ni particles.

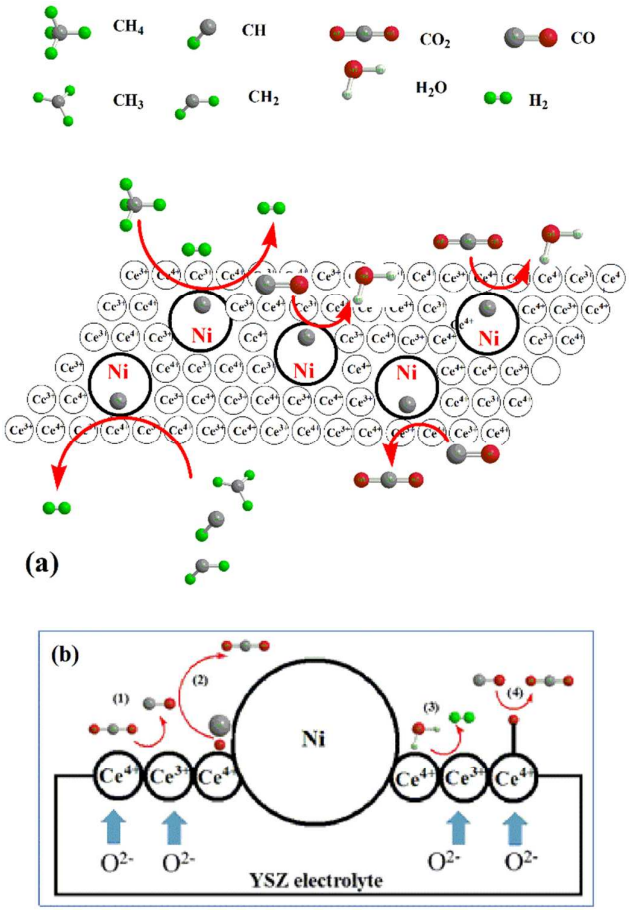

**Figure 9.** Schematic pathways of (a) carbon deposition on and (b) the removal of carbon deposits from an LSCNT anode catalyst.

The reaction equilibrium of the Boudouard reaction, which is another way to form carbon deposition, could be influenced by the lattice oxygen (Ox) on the surface of ceria (Eq 10).

$$C\text{-}A + O_x \rightarrow CO + O_{x-1} + A \quad (9)$$

$$CO + O_x \rightarrow CO_2 + O_{x-1} \quad (10)$$

The continuous consumption of CO will shift eq. (2) and eq. (3) in the reverse direction, thus carbon deposition can be suppressed. The consumed active oxygen ions could be efficiently replenished through the oxygen ion flux travelling via the YSZ electrolyte from the cathode to the anode. In addition, the $CO_2$ and $H_2O$ products could reoxidize $Ce^{3+}$ to form $Ce^{4+}$, capturing more active oxygen (as eq. 11 and eq. 12 show). A schematic representation of the process, including the removal of deposited carbon and $Ce^{3+}/Ce^{4+}$ cycling, is shown in Figure 9.

$$Ce^{3+} + CO_2 \rightarrow Ce^{4+} + CO \quad (11)$$

$$Ce^{3+} + H_2O \rightarrow Ce^{4+} + H_2 \quad (12)$$

Consequently, it is reasonable to declare that the carbon formation on surface of the catalyst was suppressed because of the oxidative environment provided by the Ce redox couple surrounding the Ni particles.

## Conclusions

A novel Ni/Ce co-doped lanthanum strontium titanate (LSCNT) perovskite composite with high-dispersed Ni surrounded by uniformly dispersed Ce species can only be obtained by sintering the material in the consecutive atmospheres of air and 10% $H_2$/Ar. The SOFC equipped with LSCNT anode shows excellent electrochemical performance and stability both in 5000 ppm $H_2S/H_2$ and in dry $CH_4$. The material also exhibited excellent long term coking and sulfur resistance. The detailed characterizations demonstrate that the presence of exsolved metallic Ni provided more active sites for the fuel oxidation reaction and the presence of widely-dispersed Ce species enclosing the Ni particles had oxygen storage ability and redox properties providing more active oxygen ions to promote the electrochemical reaction and facilitate the removal of carbon deposits formed on Ni.

## Acknowledgements

This work is supported by a Natural Sciences and Engineering Research Council (NSERC) of Canada Strategic Project Grant and the National Natural Science Foundation of China under grant 21303141.

## References

1. G. Xiao and F. Chen, *Electrochem. Commun.*, 2011, **13**, 57-59.
2. J.H. Wang and M. Liu, *J. Power Sources*, 2008, **176**, 23-30.
3. W. Wang, C. Su, Y. Wu, R. Ran and Z. Shao, *Chem. Rev.*, 2013, **113**, 8104-8151.
4. V.B. Vert, F.V. Melo, L. Navarrete and J.M. Serra, *Appl. Catal. B: Environ.*, 2012, **115-116**, 346-356.
5. L. Huang, F. Zhang, N. Wang, R. Chen and A.T. Hsu, *Int. J. Hydrogen Energ.*, 2012, **37**, 1272-1279.
6. E. Brightman, D.G. Ivey, D.J.L. Brett and N.P. Brandon, *J. Power Sources*, 2011, **196**, 7182-7187.
7. Y.F. Sun, J.H. Li, S.H. Cui, K. T. Chuang and J.L. Luo, *Electrochim. Acta*, 2015, **151**, 81-88.
8. X. Zhou, N. Yan, K.T. Chuang and J.L. Luo, *RSC Adv.*, 2014, **4**, 118-131.
9. A.L. Vincent, A.R. Hanifi, J.L. Luo, K.T. Chuang, A.R. Sanger, T.H. Etsell and P. Sarkar, *J. Power Sources*, 2012, **215**, 301-306.
10. K.J. Yoon, C.A. Coyle and O.A. Marina, *Electrochem. Commun.*, 2011, **13**, 1400-1403.
11. N. Sakai, T. Horita, K. Yamaji, Y.P. Xiong, H. Kishimoto, M.E. Brito and H. Yokokawa, *Solid State Ionics*, 2006, **177**, 1933-1939.
12. S.P. Simner, J.S. Hardy, J.W. Stevenson and T.R. Armstrong, *Solid State Ionics*, 2000, **128**, 53-63.
13. M. Mori, Y. Hiei and N.M. Sammes, *Solid State Ionics*, 2000, **135**, 743-748.
14. J.C. Ruiz-Morales, J. Canales-Vázquez, C. Savaniu, D. Marrero-López, W. Zhou and J. T.S. Irvine, *Nature*, 2006, **439**, 568-571.
15. S.P. Jiang, *Mater. Sci. Engin.: A*, 2006, **418**, 199-210.
16. L. Adijanto, V. Balaji Padmanabhan, R. Kungas, R.J. Gorte and J.M. Vohs, *J. Mater. Chem.*, 2012, **22**, 11396-11402.
17. C. Arrivé, T. Delahaye, O. Joubert and G. Gauthier, *J. Power Sources*, 2013, **223**, 341-348.
18. H. Choi, A. Fuller, J. Davis, C. Wielgus and U.S. Ozkan, *Appl. Catal. B: Environ.*, 2012, **127**, 336-341.
19. A. Trovarelli, *Catal. Rev.-Sci. Engin.*, 1996, **38**, 439-520.
20. S. McIntosh and R.J. Gorte, *Chem. Rev.*, 2004, **104**, 4845-4866.
21. H.C. Yang, M.W. Lee, H.S. Hwang, J.K. Moon and D.Y. Chung, *J. Rare Earths*, 2014, **32**, 831-836.
22. S.S.Y. Lin, D.H. Kim and S.Y. Ha, *Appl. Catal. A: Gen.*, 2009, **355**, 69-77.
23. E. Ramírez-Cabrera, A. Atkinson and D. Chadwick, *Appl. Catal. B: Environ.*, 2004, **47**, 127-131.
24. A. Kitla, O.V. Safonova and K. Fottinger, *Catal. Lett.*, 2013, **143**, 517-530.
25. X. Sun, S. Wang, Z. Wang, J. Qian, T. Wen and F. Huang, *J. Power Sources*, 2009, **187**, 85-89.
26. C. Périllat-Merceroz, G. Gauthier, P. Roussel, M. Huvé, P. Gélin and R.N. Vannier, *Chem. Mater.*, 2011, **23**, 1539-1550.
27. X.W. Zhou, Y.F. Sun, G.Y. Wang, T. Gao, K. T. Chuang, J.L. Luo, M. Chen and V.I. Birss, *Electrochem. Commun.*, 2014, **43**, 79-82.
28. W. Kobsiriphat, B.D. Madsen, Y. Wang, M. Shah, L.D. Marks and S.A. Barnett, *J. Electrochem. Soc.*, 2010, **157**, B279.
29. W. Kobsiriphat, B.D. Madsen, Y. Wang, L.D. Marks and S.A. Barnett, *Solid State Ionics*, 2009, **180**, 257-264.

30. X.C. Lu and J.H. Zhu, *Solid State Ionics*, 2007, **178**, 1467-1475.
31. J. Dong, Z. Cheng, S. Zha and M. Liu, *J. Power Sources*, 2006, **156**, 461-465.
32. M. Chen, B.H. Moon, S.H. Kim, B.H. Kim, Q. Xu and B.G. Ahn, *Fuel Cells*, 2012, **12**, 86-96.
33. V. Dusastre and J.A. Kilner, *Solid State Ionics*, 1999, **126**, 163-174.
34. Q. Fu, F. Tietz, D. Sebold, S. Tao and J.T.S. Irvine, *J. Power Sources*, 2007, **171**, 663-669.
35. J. P. Trembly, A.I. Marquez, T.R. Ohrn and D.J. Bayless, *J. Power Sources*, 2006, **158**, 263-273.
36. J. B. Wang, J.C. Jang and T.J. Huang, *J. Power Sources*, 2003, **122**, 122-131.
37. Y.F. Sun, J.H. Li, K.T. Chuang and J.L. Luo, *J. Power Sources*, 2015, **274**, 483-487.
38. J. Li, C. Wang, C. Huang, W. Weng and H. Wan, *Catal. Lett.*, 2010, **137**, 81-87.
39. G.K. Reddy, S. Loridant, A. Takahashi, P. Delichère and B.M. Reddy, *Appl. Catal. A: Gen.*, 2010, **389**, 92-100.
40. A.N.J. van Keulen, K. Seshan, J.H.B. J. Hoebink and J.R.H. Ross, *J. Catal.*, 1997, **166**, 306-314.

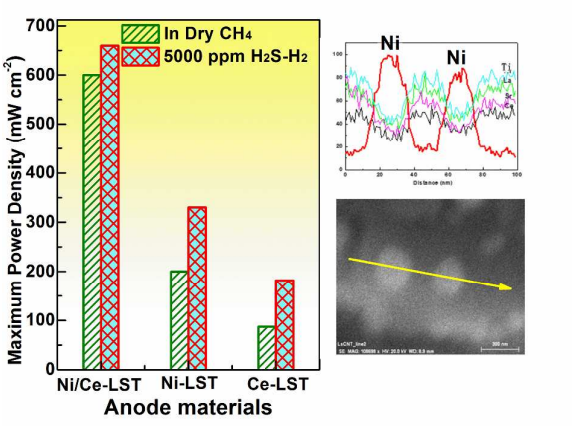


Ni/Ce co-doped lanthanum strontium titanate (LSCNT) with high-dispersed Ni surrounded by Ce species can only be obtained by sintering the material in the consecutive atmospheres of air and 10% $H_2$/Ar. The SOFC with LSCNT anode shows excellent electrochemical performance and stability both in 5000 ppm $H_2S/H_2$ and in dry $CH_4$. The presence of exsolved metallic Ni provided more active sites for the fuel oxidation reaction and the widely-dispersed Ce species enclosing the Ni particles had oxygen storage ability and redox properties and created an oxidative environment, simultaneously facilitating the electrochemical reaction and promoting the removal of carbon deposition.